Static strength analysis of a novel custom triflange acetabular component by experimental testing and finite element modelling

Riis Kaak

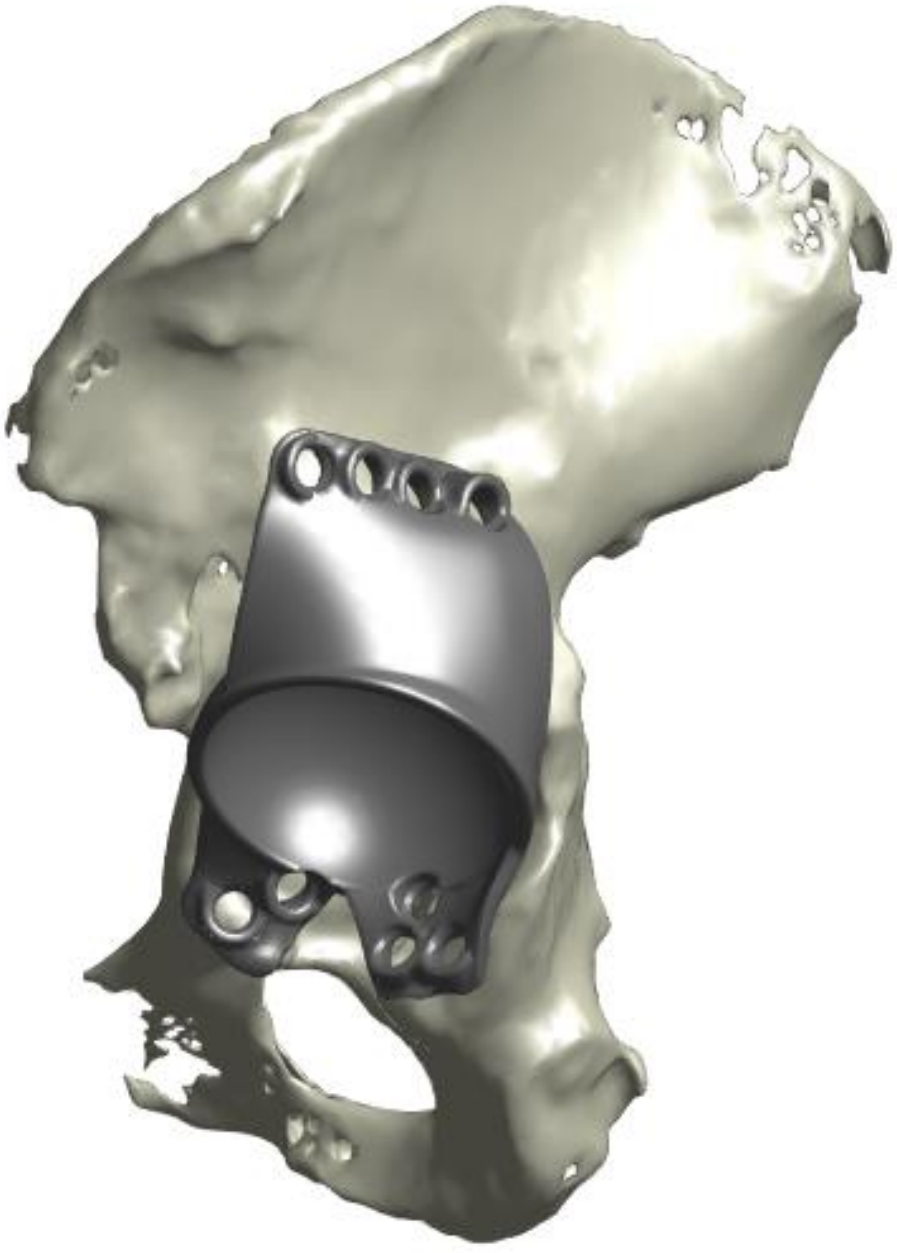

Static strength analysis of a novel custom triflange acetabular component by experimental testing and finite element modelling

BME MSc Thesis (BM51035)

Author:
Riis Kaak BSc
MSc Biomedical Engineering student
Track I: Neuromusculoskeletal Biomechanics
Student number: 5313597

TUDelft Supervisor:
Dr. Ir. Nazli Tümer

Company Supervisors:
Dr. Ir. Thom Bitter
Ir. Sjors Coenders

Orthopaedic Research Lab
www.biomechanics.nl
Institute for Health Sciences
Radboudumc

Graduation date: August 23 2022

Graduation committee members:

Dr. Ir. Nazli Tümer
Assistant Professor at TU Delft
Faculty of Mechanical, Maritime and Materials Engineering

Dr. Ir. Jie Zhou
Associate Professor at TU Delft
Faculty of Mechanical, Maritime and Materials Engineering

Ir. Sjors Coenders
Orthopaedic Engineer at the Orthopaedic Research Lab of Radboudumc

Acknowledgements

I would like to thank my supervisors Thom Bitter, Sjors Coenders, and Nazli Tümer for their valuable feedback and assistance during the project, and Richard van Swam for his technical assistance with the experiment, and Wim Rijnen for his help with cementing the cup. In particular, I would like to thank the Orthopedic Research Laboratory for giving me the opportunity to carry out this project.

Abstract

Acetabular component revision surgery in people with severe acetabular bone defect is challenging and associated with higher failure rates compared to primary total hip arthroplasty. This MSc Thesis project aimed to assess the static strength of a novel custom triflange acetabular component (CTAC) by experimental testing and finite element (FE) modelling. Experimental validation of the developed FE model showed that the simulation underestimated the axial displacement of the femoral head as well as most implant strains. However, most numerically found implant strains showed a good linear correlation with the experimentally measured implant strains. Based on the experimental and numerical results, it was concluded that the developed CTAC has sufficient static strength to resist excessive static loads in multiple physiologically relevant directions. The developed CTAC has the potential to dramatically decrease the high failure rates currently associated with acetabular component revision surgery.

Keywords: static strength analysis, custom triflange acetabular component, finite element modelling, acetabular bone defect

Contents

Chapter 1

Introduction

Total hip arthroplasty (THA) is a surgical treatment for degenerative hip joint diseases like osteoarthritis with satisfactory clinical outcomes (Karachalios, Komnos, & Koutalos, 2018). Every year, around 1.5 million procedures are performed worldwide, of which 600,000 in Europe (Dall'Ava, Hothi, Di Laura, Henckel, & Hart, 2019). The primary goal of the procedure is to regain normal biomechanical hip function and to reduce pain and discomfort caused by osteoarthritis. Failure rates at 10 years follow-up are 11.4% for primary THA (Chiarlone et al., 2020). Compared to primary THA, revision THA is a more complex procedure with inferior clinical outcomes and higher failure rates at 10 years follow-up of 25.6% (Chiarlone et al., 2020). Furthermore, 58% of hip revision operations comprise acetabular component revisions (Lie, Havelin, Furnes, Engesaeter, & Vollset, 2004). The high degree of variation in the amount and quality of the remaining bone stock make acetabular component revisions particularly challenging (Sheth, Nelson, Springer, Fehring, & Paprosky, 2013).

Existing treatment options have been shown to be unpredictable and provide unsatisfactory clinical and radiological outcomes in the management of severe acetabular bone defect (Chiarlone et al., 2020). Therefore, there is a strong need for the development of a novel acetabular revision implant that is capable of taking patient-specific bone architecture into account. In the last few decades, metal 3D printing of custom triflange acetabular components (CTACs) has increased in popularity as a treatment option for acetabular component revision in people with severe acetabular bone defect (Chiarlone et al., 2020). CTACs are designed using patient's CT data to match the implant to the patient's pelvic geometry, often in consultation with an orthopaedic surgeon to aid in screw positioning. Even for severe acetabular bone defects classified as AAOS type III or IV and Paprosky type IIIA or IIIB, CTACs are a reliable

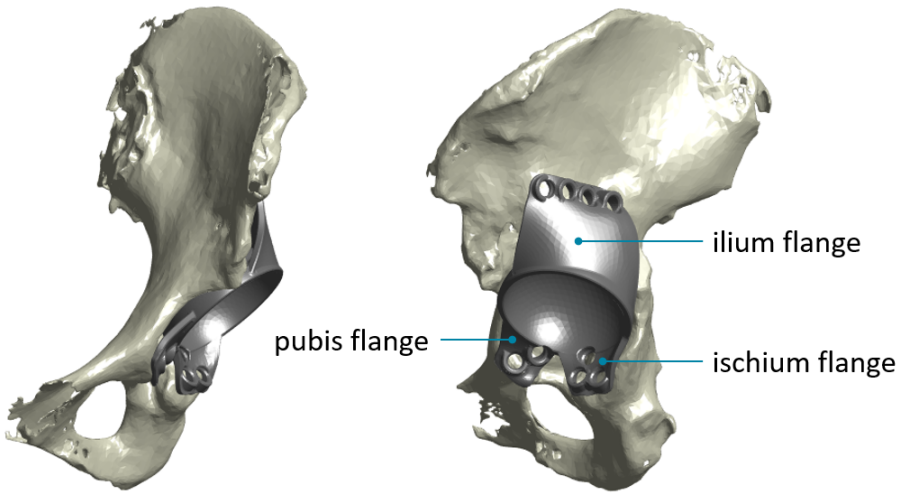

Figure 1.1: Front view (left) and lateral view (right) of the developed custom triflange acetabular component (grey) positioned in a segmented left hemipelvis (ivory).

solution with satisfactory clinical outcomes at midterm follow-up and with reported survival rates of around 90% (De Martino et al., 2019; Chiarlone et al., 2020).

Recently, a type of CTAC for use in acetabular component revision surgery in people with severe acetabular bone defect was developed in-house at the Orthopaedic Research Lab (ORL) at the Radboudumc in Nijmegen, The Netherlands, see Figure 1.1. As an initial step in the development process, the novel implant design has to undergo preliminary experimental testing and finite element (FE) analysis to assess the static implant design performance. FE modelling is a widely used technique for evaluation of implant design performance under various loading conditions. It has previously been applied to analyse the stress-strain state of acetabular components for revision surgery (Kaku, Hara, Tabata, & Tsumura, 2015; Plessers & Mau, 2016). More recently, FE models have been developed of custom acetabular components for revision surgery (Borovkov et al., 2018; Maslov et al., 2019; Doczi, Szoedy, & Zwierczyk, 2020; Moussa, Rahman, Xu, Tanzer, & Pasini, 2020). However, not one of these FE models was experimentally validated. Experimental validation of an FE model is pivotal to assessing the model's accuracy and to enabling improvement of the FE model. This MSc Thesis project aims to assess the static strength of the developed CTAC. To that aim, the implant will be loaded with an excessively high static load in a physiologically relevant direction. Also, an FE model of the developed CTAC will be experimentally validated. Lastly, the static strength of a 3 mm thick implant design will be compared with a 4 mm thick implant design.

Chapter 2

Methods

The followed workflow in this study is depicted in Figure 2.1. Two implants were designed: a 3 mm thick implant and a 4 mm thick implant. The thickness of 4 mm was based on regular clinical practice. The 3 mm implant was manufactured for experimental testing. It was chosen to manufacture the 3 mm implant because in the future a 1 mm porous layer may be added to enhance bone ingrowth, so testing the 3 mm thick implant would be a kind of worst-case scenario. The experimental conditions were mimicked as close as possible in an FE model of the 3 mm implant. For the experimental validation, the results from the experiment with the 3 mm implant were compared to the results from the FE model with the 3 mm implant. To compare the stress states of the 3 mm and 4 mm implants, four different loading conditions were used, including the loading condition for experimental validation.

First, the development of the FE model with the 3 mm implant for experimental validation will be explained. Second, the development of the experiment with the 3 mm implant for experimental validation will be described. Third, the development of the FE model with the 4 mm implant will be clarified. Finally, the applied loading conditions for comparison of the 3 mm with the 4 mm implants will be covered.

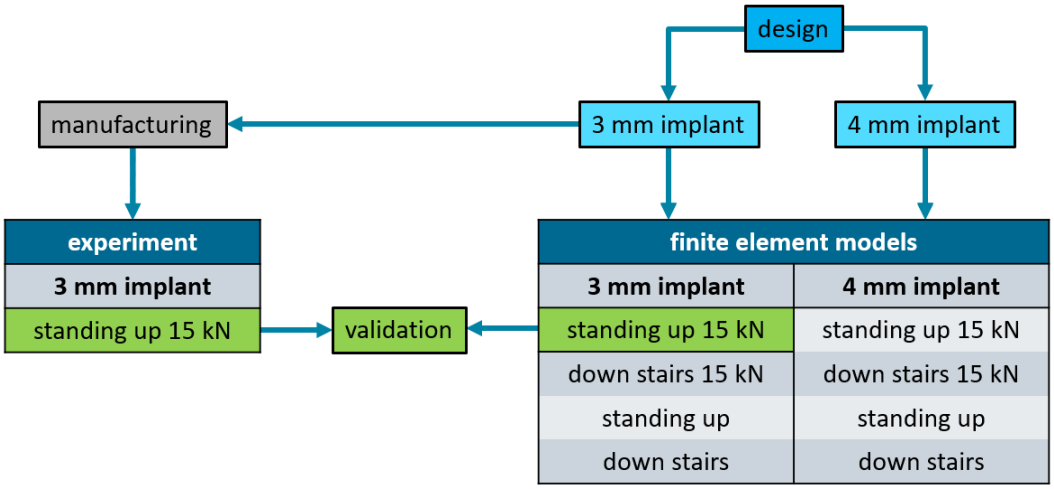

Figure 2.1: Schematic representation of the followed workflow in this study. Two implant designs were designed: a 3 mm thick implant and a 4 mm thick implant. The 3 mm thick implant was manufactured for experimental testing. Four different loading conditions were used to compare the 3 mm and 4 mm thick implants.

2.1 Validation

2.1.1 The FE model

The first step in the development of the FE model of the 3 mm implant used for experimental validation, was the computer aided design of 11 screws, see Figure 2.2. Synthes cancellous screws (418.035) were used for implant fixation (SYNTHES, n.d.). This type of screw is 35 mm in length and has a nominal thread diameter of 6.5 mm. SolidWorks 2020 was used to obtain a 3D model of the screw geometry, which complied with the relevant standard for screws with a deep thread, i.e. cancellous screws, and a nominal thread diameter of 6.5 mm (ISO 5835:1991) (ISO, n.d.). The screw thread was modelled as a cylinder with a diameter equal to the nominal thread diameter of 6.5 mm, in accordance with similar FE studies (Kaku et al., 2015; Maslov et al., 2019; Doczi et al., 2020; Borovkov et al., 2018; Fu et al., 2018; Hsu et al., 2007). For each of the 11 screw holes in the implant, a screw was positioned in place (HyperMesh 2020, HyperWorks, AltairEngineering, Inc. Troy, MI).

The second step was the generation of the geometries for the cement layer, the cup, and the femoral head (HyperMesh 2020, HyperWorks, AltairEngineering, Inc. Troy, MI), see Figure 2.3. All three hemispheres originated from the same point in space

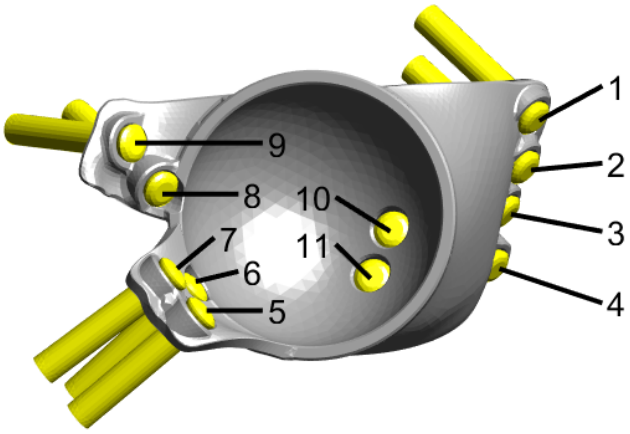

Figure 2.2: Top view of the 3 mm thick implant (grey) and the 11 screws (yellow).

as the implant's hemisphere. The cement and cup were made as hollow hemispheres, and the head was made as a solid hemisphere. The outer and inner cement diameters were 54 mm and 50 mm, respectively, the outer and inner cup diameters were 50 mm and 32 mm, respectively, and the head diameter was 32 mm. All aforementioned dimensions of the cement, cup, and head were based on advice of an experienced orthopaedic surgeon. The aforementioned geometries of the implant, screws, cement, cup, and head were all positioned in the original CT scan in which the pelvis was segmented, see Figure 1.1.

To test the implant in the experiment, it was needed to apply a high hip reaction force in a physiologically meaningful direction. To that aim, hip reaction forces in % body weight of nine daily activities were obtained from the OrthoLoad HIP98 database (OrthoLoad, n.d.). The hip reaction forces from the HIP98 database act on the left hip centre of rotation (HCOR) and are expressed in a specific pelvis coordinate system based on the left HCOR, the right HCOR, and the centre of the L5-S1 joint. The centre of the implant's hemisphere was used as the left HCOR. The right HCOR and the centre of the L5-S1 joint were determined from the available CT scan. The implant, screws, cement, cup, and head were transformed from their original position in the CT scan coordinate system to the HIP98 pelvis coordinate system (OrthoLoad, n.d.). The orientation of the maximum resultant force vector during the standing up activity was chosen as the axial loading direction for the experiment with the 3 mm implant. This orientation was chosen because preliminary tests showed that it yielded the highest implant strains of all available maximum resultant force vector orientations of the HIP98 database. For the FE model, the implant, screws, cement, cup, and head were transformed from the HIP98 pelvis

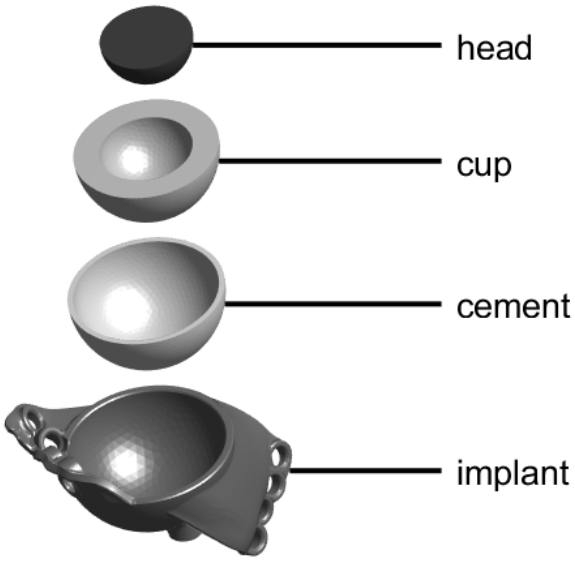

Figure 2.3: Exploded view of the hemispherical head, cup, and cement geometries relative to the implant.

coordinate system such that the final negative Z-axis pointed in the same direction as the orientation of the maximum resultant force vector during the standing up activity.

The final step in the development of the FE model was the design of a block based on the geometry of the segmented left hemipelvis for which the implant was custom-made. The block primarily served to fixate the implant with the 11 screws. To facilitate milling of the block, the pelvic geometry was cut with planes to introduce flat surfaces. Also, these flat surfaces allowed for proper fixation of the block during the experiment. Lastly, space was created under and behind the implant by removal of the pelvic geometry to allow for implant strain measurements with strain gauges during the experiment. Most importantly, the pelvic geometry was maintained at the locations where the flanges were in contact with the pelvic bone geometry. The last step of making the block for the FE model was to subtract the volumes taken up by the 11 cylindrical screw threads from the block volume by performing a Boolean operation. The final block is shown in the top of Figure 2.4.

The final FE model consisted of six solid components: the block, the 11 screws, the implant, the cement, the cup, and the head, see Figure 2.4. All components were meshed with 2 mm linear four-node tetrahedral solid elements based on surface deviation, which allowed for smaller elements near e.g. the screw holes (Plessers & Mau, 2016; Dong et al., 2018). The mesh properties of the model and its components

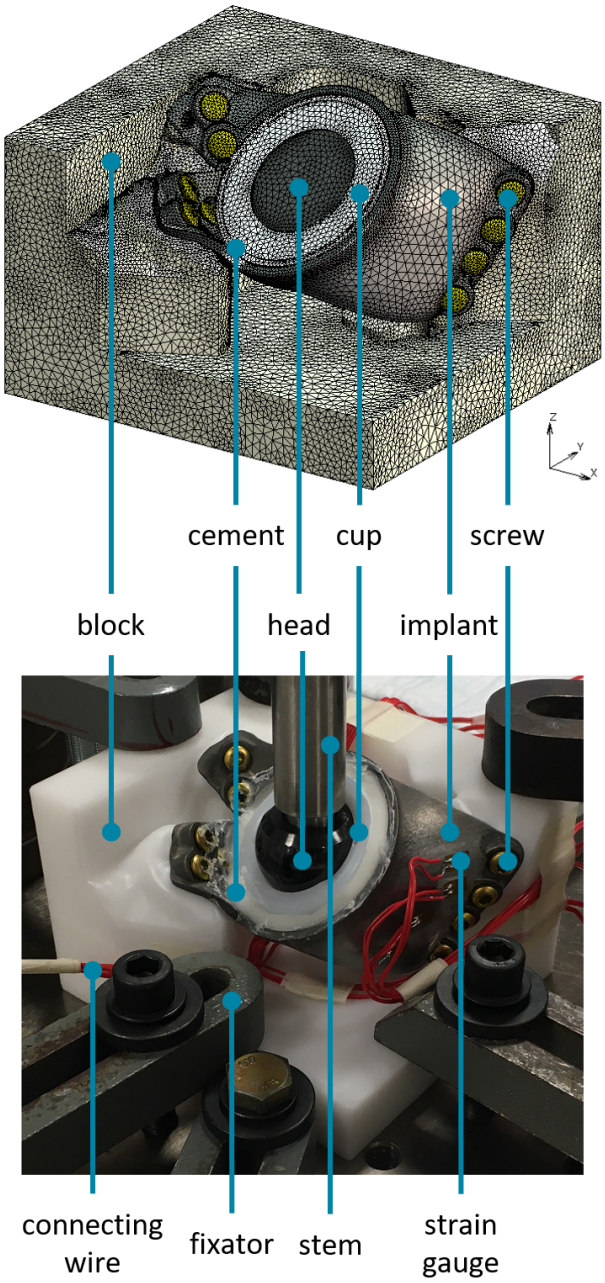

Figure 2.4: The finite element model with the coordinate system (top) and the experimental setup (bottom). The six components that the finite element model and the experimental setup have in common are shown in the middle. The additional components of the experimental setup are shown at the bottom.

are shown in Table 2.2. The model consisted of materials with homogeneous, linear elastic, and isotropic properties, see Table 2.1. Marc Mentat (Marc Mentat 2021.4, MSC Software Corporation, Santa Ana, CA, USA) was used for performing the simulations. The model was fixed in the X-, Y-, and Z-direction at the nodes at the bottom surface of the block. All components were considered glued, so no friction was allowed (Borovkov et al., 2018; Hsu et al., 2007; Doczi et al., 2020; Fu et al., 2018; Kaku et al., 2015). The implant was loaded in the negative Z-direction on a femoral head node with coordinates (0,0,0), which corresponded to the centre of the implant, cement, cup, and head hemispheres. The axial load magnitude increased from 0 kN to 15 kN in 30 steps of 500 N.

Table 2.1: Material properties of the 3 mm and 4 mm implant finite element models.

Component	**Material**	$\boldsymbol{E}$ **(MPa)**	$\boldsymbol{v}$ **(-)**
Block	Delrin	2,943[1]	0.35[2]
Screws	CP Ti	103,000[3]	0.34[3]
Implant	3D printed Ti6Al4V	122,000[4]	0.3[5]
Cement	PMMA	2,000[6]	0.4[7]
Cup	UHMWPE	1,000[8]	0.46[8]
Head	Oxinium	97,900[9]	0.3[9]

References: [1]DSGROUP (n.d.), [2]SPACEMATDB (n.d.), [3]ASMINTERNATIONAL (n.d.), [4]3DSYSTEMS (n.d.), [5]Kadkhodapour et al. (2015), [6]Lee (n.d.), [7]Orr, Dunne, and Quinn (2003), [8]Malito et al. (2018), [9]Innocenti et al. (2014).

Table 2.2: Mesh properties of the 3 mm implant finite element model.

Component	**Number of elements**	**Number of nodes**
Block	404,809	77,009
Screws	98,917	21,560
Implant	127,005	26,545
Cement	12,945	3,687
Cup	25,110	5,301
Head	9,970	2,149
Total	678,756	136,251

2.1.2 The experiment

For the design of the block used in the experiment, a similar Boolean operation was performed as for the block used in the FE model, but with 3.2 mm diameter cylinders instead of 6.5 diameter cylinders to predrill the screw thread positions during milling. The preparation of the experimental setup consisted of the following four steps: 1) Surface preparation and strain gauge installation, 2) tightening the screws, 3) cementing the cup, and 4) placing the block in the MTS machine.

1) Surface preparation and strain gauge installation

For the preparation of the implant surface and the installation of the strain gauges, the steps as described in Micro-Measurements' Instruction Bulletins B-127 and B-129-8 were followed precisely (Micro-Measurements, n.d.-n; PG, n.d.). A total of 12 linear strain gauges of the type CEA-06-062UWA-350 were installed on the implant's surface, see Figure 2.5. The centres of the strain gauges' measuring grids corresponded to the locations of nodes at which relatively high maximum principal elastic strain values were expected based on the FE model's simulation results (Du Preez, Monaheng, Haupt, & Olwagen, 2016). The orientations of the strain gauges corresponded to the orientations of the maximum principal strains at the corresponding nodes. To facilitate installation of the strain gauges at the correct location and in the correct orientation, two 3D printed polyamide (Oceanz, Ede, The Netherlands) strain gauge placement guides were used, see Figure 2.5. After the installation of all 12 strain gauges, each strain gauge was soldered to a connecting wire, see Figure 2.4. Each connecting wire was marked with a number corresponding to the strain gauge number to which it connected.

2) Tightening the screws

11 Synthes cancellous bone screws (418.035) were screwed in the block with a drill to fixate the implant (SYNTHES, n.d.). This step was done in three stages: 1) positioning a screw in each of the three flanges; 2) placing the two cup screws; 3) screwing in the remaining six flange screws (Medical, n.d.).

3) Cementing the cup

Next, a STRYKER Exeter Rimfit X3 Acetabular Cup (6309-3-250) with an outer and inner cup diameter of 50 mm and 32 mm, respectively, was cemented into the implant by an experienced orthopaedic surgeon (STRYKER, n.d.-a). The cup has four PMMA cement spacers that allow for a 2 mm thick cement layer. STRYKER

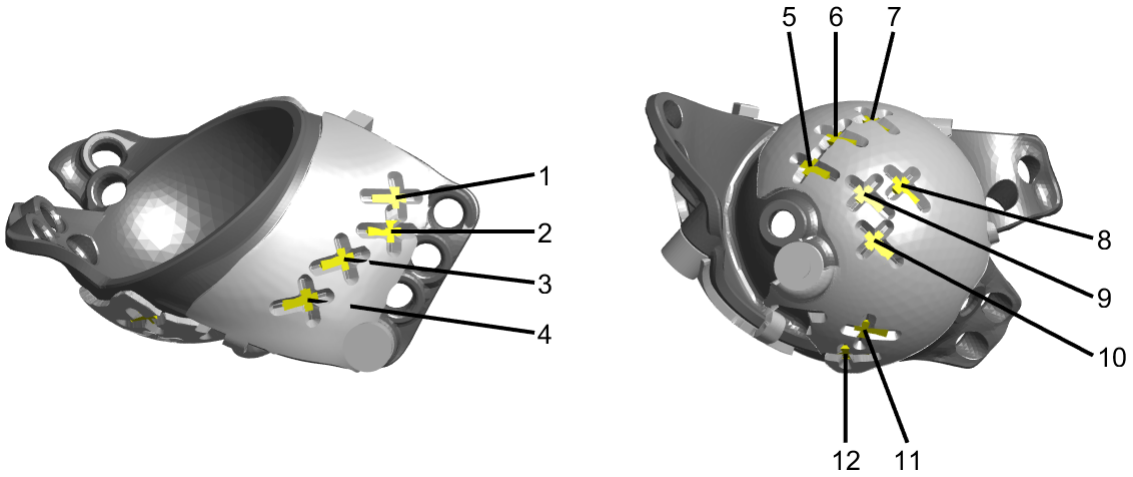

Figure 2.5: Numbering of the 12 locations for strain measurement on the implant (grey) with the 12 strain gauges (yellow), shown together with the two strain gauge placement guides (white). Left: side view of the four locations for strain measurement on the ilium flange and the ilium strain gauge placement guide; Right: bottom view of the eight locations for strain measurement on the implant's outer hemisphere and the placement guide for the outer hemisphere.

Simplex Bone Cement was used for cementing the cup into the implant (STRYKER, n.d.-b).

4) Placing the block in the MTS

Finally, the entire setup was positioned in an MTS machine (MTS DSTS 3301, 458.20 micro-console, MTS Systems Corporation, Eden Prairie, MN) by fitting a 32 mm diameter Smith&Nephew OXINIUM femoral head (SmithandNephew, n.d.) into the cemented cup. The femoral head was connected to the MTS machine with a custom-made connecting stem, see Figure 2.4. The block was fixed to the bottom plate of the machine by means of 7 fixators, see Figure 2.4. The connecting wires were soldered to RJ50 UTP cables. Again, these cables were marked with a number corresponding to the strain gauge number they were connected to. Finally, all cables were connected to the MTS machine for data acquisition. Similar to the loading condition in the FE model, the implant was loaded in the negative Z-direction from 0 kN to 15 kN in 30 steps of 500 N. The test protocol started out with a one-minute loading of 0 N, after which the loading was increased 30 times with 500 N steps to a final axial loading of 15 kN. Each force level was maintained for one minute to allow for later averaging of the strain gauge data over time. During the experiment, the axial displacement

and axial force were measured at the MTS load cell. All data were recorded at a frequency of 87.5 Hz. The experiment was carried out at room temperature and a humidity of 65%.

Apart from the main experiment described above, an additional experiment was carried out after completion of the main experiment. This additional experiment was needed to measure and later correct for all axial displacements happening inside the long rod of connecting components above the centre of the femoral head. For this additional experiment, all parts including the femoral head and stem were removed from the MTS machine. At the beginning of this experiment, the bottom of the rod of connecting components touched a pile of metal disks positioned in the MTS. The same aforementioned protocol of load application was followed.

2.2 3 mm versus 4 mm thick implant

For the development of the FE model of the 4 mm implant, the same steps were followed as for the development of the FE model of the 3 mm implant used for experimental validation, as described above. The increase in implant thickness did not affect the dimensions of the cement, cup, and head, because the implant thickness was increased at the implant's outer hemisphere. However, regarding the flanges, the contact surface with the bone had to be maintained. Because of this, the implant thickness at the flanges increased at the superior side where the implant was in contact with the screw heads. This increased the distance from the pelvic surface to the screw holes and affected the screw positioning in space. Therefore, the screws were positioned separately for the 3 mm and 4 mm implants.

For comparison of the stress states of the 3 mm with the 4 mm implant, four different loading conditions were used, see Figure 2.1 and Figure 2.6. The first loading condition was the same loading condition as applied to the 3 mm implant model used for experimental validation: from 0 kN to 15 kN in 30 steps of 500 N in the direction of the maximum resultant force vector during the standing up activity, see Figure 2.6a. For application of the other three loading conditions, the same FE models were used. The models only differed in the orientation and magnitude of the applied load. The second loading condition was applied in the direction of the maximum resultant force vector during the down stairs activity from 0 kN to 15 kN in 30 steps of 500 N, see Figure 2.6b. The final two loading conditions consisted of the application of one full cycle of the standing up activity, see Figure 2.6c, and one full cycle of the down stairs activity, see Figure 2.6d, to compare the performance of the implant designs

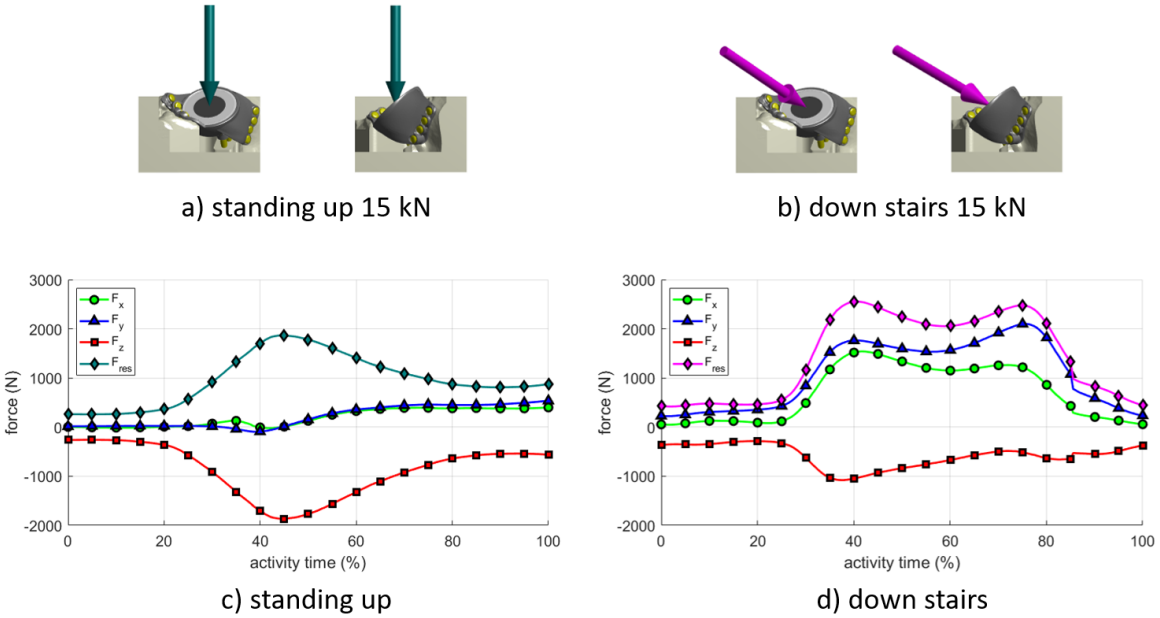

Figure 2.6: The four different loading conditions used for comparison of the 3 mm with the 4 mm thick implants. a) The experimental loading, i.e. a 15 kN load in the direction of the maximum resultant force vector during the standing up activity; b) A 15 kN load in the direction of the maximum resultant force vector during the down stairs activity; c) One full cycle of the standing up activity; d) One full cycle of the down stairs activity.

in activities of daily living. The orientations of the maximum resultant force vectors of the standing up and down stairs activities are representative of the orientations of the maximum resultant force vectors of all nine available HIP98 database activities. For each of the two activity cycles, 21 time points were picked at 5% activity time intervals.

2.3 Data analysis

2.3.1 Validation

Experimental validation of the FE model consisted of two steps: 1) comparison of the force-displacement curves of the femoral head and 2) comparison of the implant's surface strains. The axial displacement data for the force-displacement curve of the FE

model was obtained from the head node at (0,0,0), which corresponded to the centre of the femoral head hemisphere. The axial displacement data for the force-displacement curve of the experiment was obtained by recording the axial displacement and axial force during the experiment. For the implant's surface strains of the FE model, the maximum principal values of elastic strain were obtained at the nodes corresponding to the centres of the measuring grids of the strain gauges. The implant's surface strains during the experiment were obtained from the strain gauge data. For each load, the strain gauge data was averaged over time in a 50 seconds interval running from five seconds after the start of the load until five seconds before the end of the load. A regression line was made for all locations combined (Zhang et al., 2010) to serve as a more global way of validating the FE model. Additional regression lines were made for each of the 12 locations individually to locally assess the validity of the model. All data were saved as .txt files and converted to .mat files for analysis in MATLAB (Release 2020a, The Mathworks, Inc., Natick, MA, USA).

2.3.2 3 mm versus 4 mm thick implant

To compare the stress states of the 3 mm with the 4 mm implant design, the 99th percentile von Mises stresses in the implant were computed for each of the four loading conditions. The 99th percentile von Mises stress in the implant is defined as the peak von Mises stress value in the implant after exclusion of 1% of the total surface area with the highest von Mises stresses (Speelman et al., 2008). The 99th percentile von Mises stress is a more reliable measure of the implant's stress state compared to the peak von Mises stress, because the 99th percentile value is insensitive to small geometrical variations and eliminates numerical errors (Speelman et al., 2008; Plessers & Mau, 2016).

Chapter 3

Results

3.1 Validation

Figure 3.1 shows the force-displacement curves for the FE model and the experiment. At the end of the simulation (FE), the maximum axial displacement was -0.43 mm. For the experiment, two lines are shown: an unadjusted force-displacement curve (EXP) and a force-displacement curve that was adjusted for all axial displacements happening inside the long rod of connecting components above the centre of the femoral head (EXP_{adj}). The maximum axial displacements were -2.28 mm and -1.80 mm for the unadjusted and adjusted curves, respectively. Therefore, the absolute difference in maximum axial displacement between the FE model and the adjusted experimental curve was 1.37 mm.

Figure 3.2 shows the regression lines for all 12 strain measurement locations. The properties of all 12 regression lines are shown in Table 3.1. Most regression lines had a value for the coefficient of determination R^2 of 0.98 or higher. The regression lines for location 1 (FE=0.82·EXP-14.63, R^2=0.980) and location 2 (FE=0.93·EXP-24.96, R^2=0.984) had the best agreement between the FE model and the experiment and were close to the ideal values of slope = 1 and $R^2 = 1$. Locations 3, 4, and 5 stood out because of their relatively low values for R^2 of 0.444, 0.629, and 0.782, respectively. Therefore, these locations were considered outliers when computing the regression line for all locations combined, see Figure 3.3. The regression equation showed that the FE modelling results had a good linear correlation with the experimental results (FE=0.32·EXP+54.9, R^2=0.76). However, for most locations, the FE model underes-

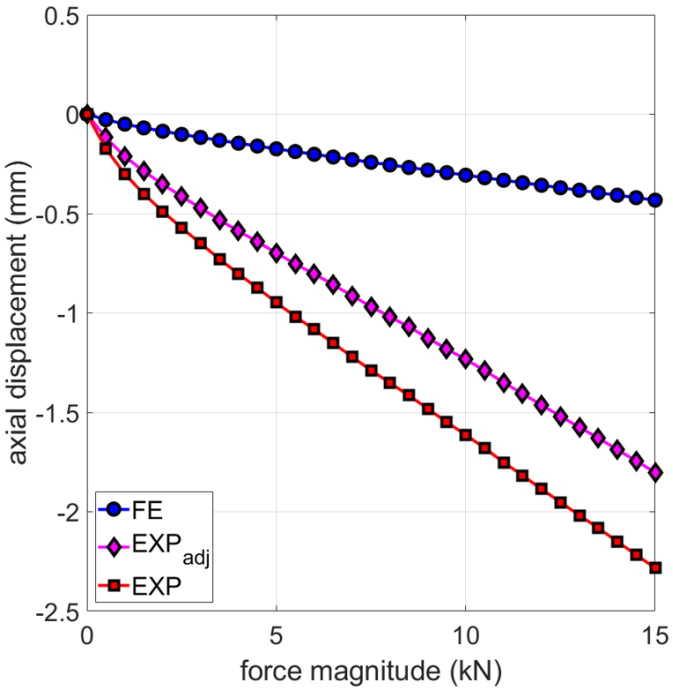

Figure 3.1: Force-displacement curves for the FE model and the experiment. EXP_{adj} was adjusted for all axial displacements happening above the centre of the femoral head.

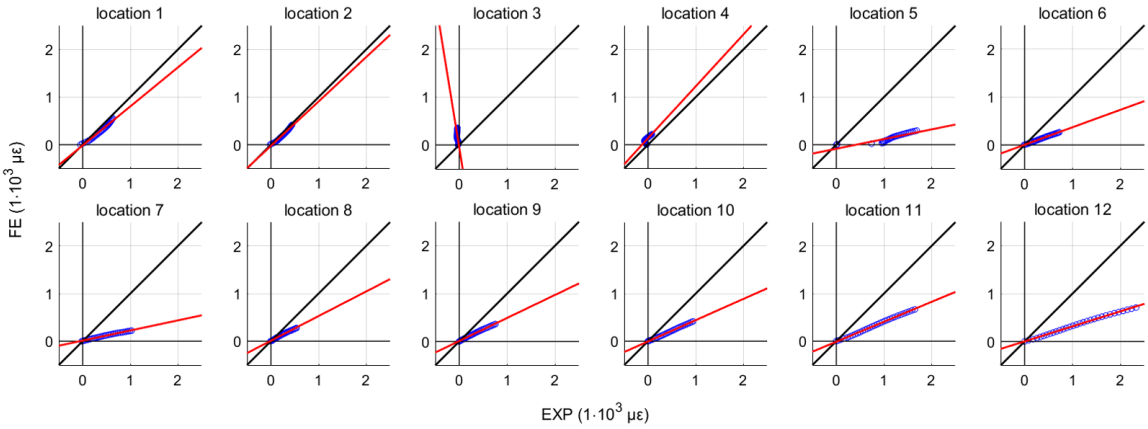

Figure 3.2: Regression lines (red) for all 12 locations. The strains from the finite element simulation are shown as FE on the y-axis. The experimentally measured strains are shown as EXP on the x-axis. The data points (N = 31) for each load are shown as open blue circles.

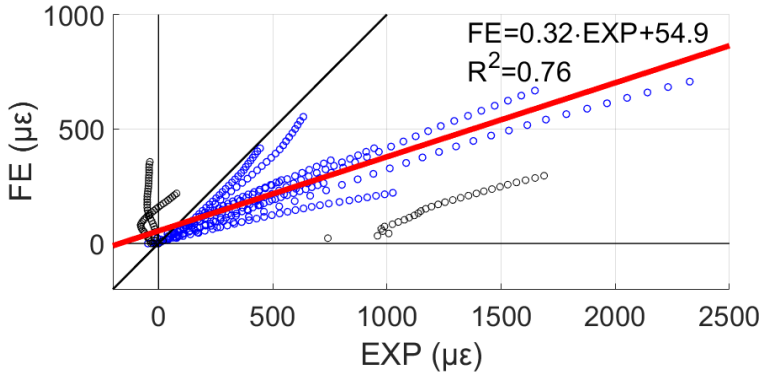

Figure 3.3: Regression line (red) for the nine locations combined. The strains from the finite element simulation are shown as FE on the y-axis. The experimentally measured strains are shown as EXP on the x-axis. The data points (N = 279) for each load and location are shown as open blue circles. The data points for locations 3, 4, and 5 were considered outliers (open black circles) and were not taken into account in the computation of the regression line.

timated the strains by more than half. The experimental strain gauge measurements, at the locations used for the computation of the aforementioned regression line, had an average standard deviation of 1.90 με.

Table 3.1: Fitted regression lines between the finite element model and the experimentally measured data for all 12 locations.

location	**FE = a·EXP + b**		$\mathbf{R^2}$
	a	**b**	
1	0.82	-14.63	0.980
2	0.93	-24.96	0.984
3	-6.17	-50.76	0.444
4	1.09	136.26	0.629
5	0.20	-84.72	0.782
6	0.37	4.07	0.999
7	0.21	12.74	0.995
8	0.52	9.57	0.994
9	0.48	9.58	0.998
10	0.45	-4.00	0.999
11	0.42	-10.51	0.999
12	0.31	1.83	0.998

3.2 3 mm implant versus 4 mm implant

In Table 3.2, the 99th percentile von Mises stresses in the 3 mm and 4 mm implants are shown for the simulations with the maximum resultant force vector orientations of the standing up and down stairs activities at 5 kN, 10 kN, and 15 kN. The 3D printed Ti6Al4V implant's yield strength $R_{p0.2}$ of 890 MPa (3DSYSTEMS, n.d.) was used to express the 99th percentile von Mises stress at the 15 kN load as a percentage of the implant's yield strength. For both activities and both implants, the 99th percentile von Mises stress increased with force magnitude. Furthermore, for both activities and for each force magnitude, the 99th percentile von Mises stress was higher for the 3 mm implant than for the 4 mm implant. Also, for both activities, the absolute difference between the 3 mm and 4 mm implant increased with force magnitude. At the 15 kN load, for both activities and both implant types, the 99th percentile von Mises stresses remained well below the implant's yield strength. At the 15 kN load, the 99th percentile von Mises stresses were 37% and 29% higher in the 3 mm implant than in the 4 mm implant for the standing up and down stairs activities, respectively.

Contour plots of the von Mises stress in the 3 mm and 4 mm implant for the standing up 15 kN and the down stairs 15 kN loads are shown in Figure 3.4. When comparing the contour plots of the 3 mm implant with the 4 mm implant, it can be seen that the contour plots of the 4 mm implant show lower stresses, i.e. the implant is much bluer. Peak stresses seem to arise mostly near the screw holes and at the junctions of the implant's hemisphere and the flanges, especially between the ischium and ilium flanges.

In Figure 3.5, the 99th percentile von Mises stresses are shown for the 3 mm and

Table 3.2: The 99th percentile von Mises stresses (MPa) in the 3 mm and 4 mm thick implants in the finite element simulations with the maximum resultant force vector orientations of the standing up and down stairs activities at 5 kN, 10 kN, and 15 kN. For the 15 kN load, the percentage of the implant's yield strength is given between brackets.

activity	**implant**	**5 kN**	**10 kN**	**15 kN (%$R_{p0.2}$)**
standing up	3 mm	96	185	268 (30%)
	4 mm	72	136	196 (22%)
down stairs	3 mm	94	178	260 (29%)
	4 mm	74	141	202 (23%)

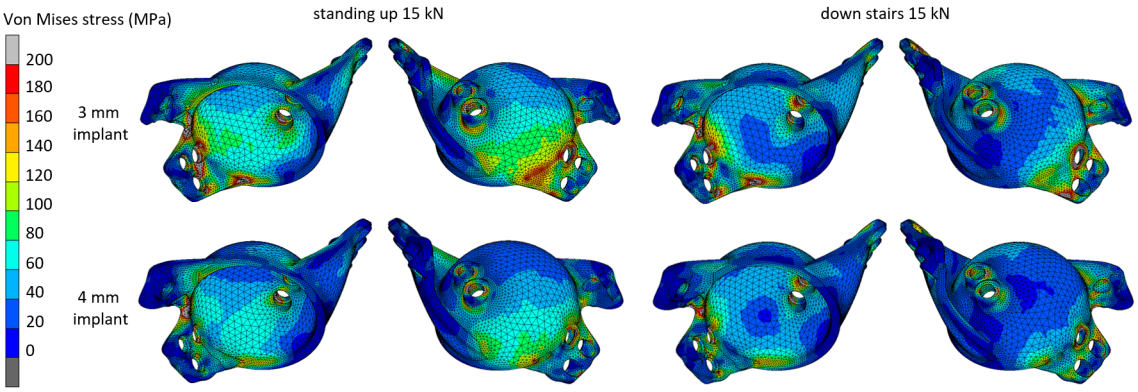

Figure 3.4: Contour plots of the von Mises stresses in the 3 mm (top row) and 4 mm (bottom row) implant when loaded with a magnitude of 15 kN in the direction of the maximum resultant force vector of the standing up activity (left column) and the down stairs activity (right column). For each of the four simulation results, a top view of the implant is shown on the left and a bottom view of the implant is shown on the right.

4 mm implant for the down stairs and standing up activities as a function of the activity time. For both activities, the 99th percentile von Mises stress was always lower in the 4 mm implant than in the 3 mm implant. The 99th percentile von Mises stress values showed a pattern similar to the absolute resultant force of the respective activity, see Figure 2.6c and Figure 2.6d. Higher 99th percentile von Mises stresses were found in the down stairs activity than in the standing up activity.

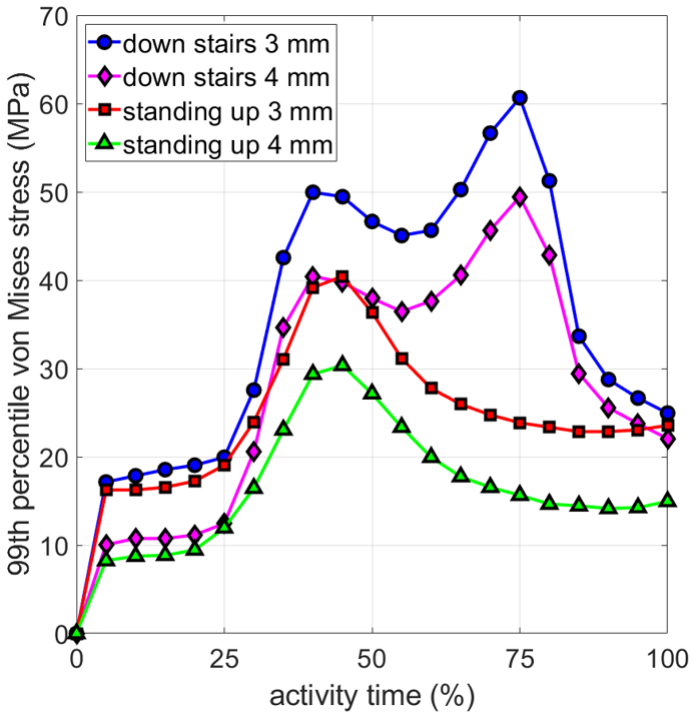

Figure 3.5: The 99th percentile von Mises stress during the down stairs and standing up activities for the 3 mm and 4 mm thick implants shown as a function of the activity time (%).

Chapter 4

Discussion

4.1 Validation

The first step in validating the FE model was the comparison of the force-displacement curve of the experiment with the force-displacement curve of the FE model. Figure 3.1 shows that the maximum axial displacement was 1.37 mm larger in the adjusted experimental curve compared to the FE model.

The second strep in validating the FE model was the fitting of linear regression lines between the simulation data and the experimental data. For some locations like 1 and 2 the experimentally measured strains were well in accordance with the simulation results. However, for the computation of the regression line between the simulation data and the experimental data of all locations, shown in Figure 3.3, locations 3, 4, and 5 were left out because they showed different behaviour as compared to the other locations. Furthermore, they were strongly deviant from the expected strain behaviour based on the FE model simulation results. For the strain gauge installed at location 5, it was noted that after setting the signal to zero the day before the experiment, it had climbed up towards a few hundreds of $\mu\epsilon$ whereas all others had increased only by a few $\mu\epsilon$. It is unknown what might have caused this behaviour. Regarding the strain gauges installed at locations 3 and 4, these seem to have measured compression during the experiment, while they were expected to measure tension. A possible explanation for these experimental findings could be that the directions of the maximum principal elastic strains predicted by the FE model were incorrect at these locations. This would have caused the strain gauges to measure strain in a direction

slightly more perpendicular to the actual direction of the maximum principal elastic strain, which would have resulted in these strain gauges measuring compression.

The remaining locations 6, 7, 8, 9, 10, 11, and 12 at the implant's outer hemispherical surface showed good linear correlations with the FE model simulation results, see Table 3.1. However, for these locations, the FE model underestimated the experimentally measured strains by more than half.

All in all, the experimental axial displacement was greater than predicted by the FE model, most locations showed good linear correlations, and most experimentally measured implant strains were larger than those of the FE model, especially at the implant's outer hemispherical surface. However, the finding that the axial displacement was greater for the experiment than for the FE model, is in agreement with the finding that most experimentally measured implant strains were higher than the FE model implant strains. There are a few possible explanations for the aforementioned differences between the experimental results and the FE model simulation results, as will be described below.

4.1.1 FE model: contact at the screw-implant, block-implant and screw-block interfaces

First and foremost, it is likely that the FE model overestimated the strength of the screw fixations. In the FE model, contact at the screw-implant interface was defined as glued. Although it is common in existing FE models of revision acetabular components fixed with screws to glue this contact interface (Fu et al., 2018; Kaku et al., 2015; Hsu et al., 2007), this way of modelling screw-implant contact limits implant movement near the screw holes. Some existing FE models of revision acetabular components fixed with screws do allow friction at the screw-implant interface (Borovkov et al., 2018; Doczi et al., 2020), but none of all aforementioned FE models was validated by experiment. For the FE model used in this study, allowing friction with a coefficient of 0.2 at the screw-implant interface, yielded a maximum axial displacement of -0.57 mm, which is an increase in axial displacement of 0.14 mm compared to the original FE model. It is theoretically justified to allow friction at the screw-implant interface in the case of non-locking head screws, which are screws without a threaded screw head and corresponding threaded implant screw holes, i.e. the screws used in this study (C.-H. Chen, Hung, Hsu, Chen, & Chiang, 2017).

Regarding the block-implant interface, some similar FE models have glued this in-

terface (Fu et al., 2018; Kaku et al., 2015), whereas others allowed frictional contact (Borovkov et al., 2018; Doczi et al., 2020; Hsu et al., 2007). There is no experimental evidence for the use of either glued contact or frictional contact at this interface. For the FE model used in this study, allowing friction with a coefficient of 0.2 at the block-implant interface, yielded a maximum axial displacement of -0.43 mm. This was not different from the axial displacement of the original FE model. Allowing friction with a coefficient of 0.2 at the screw-implant and block-implant interfaces, yielded a maximum axial displacement of -0.58 mm. This meant an increase in axial displacement of 0.01 mm compared to the original FE model with only frictional contact at the screw-implant interface. Thus, allowing friction at the screw-implant and block-implant interfaces managed to decrease the difference in maximum axial displacement between the adjusted experimental curve and the original FE model by 0.15 mm to -1.22 mm. The increase in axial displacement of the FE model is primarily caused by allowing friction at the screw-implant interface, and to a much lesser extent by allowing friction at the block-implant interface.

Regarding the screw-block contact interface, which was also glued in the FE model in this study, there is some experimental evidence that justifies this approach (Inzana, Varga, & Windolf, 2016; Wieding, Souffrant, Fritsche, Mittelmeier, & Bader, 2012). Furthermore, all current FE models similar to the one used in this study have in common that this interface is glued (Borovkov et al., 2018; Maslov et al., 2019; Doczi et al., 2020; Fu et al., 2018; Kaku et al., 2015; Hsu et al., 2007). This is generally done to compensate for the missing screw thread of the cylindrical screw shafts. Glued contact at this interface therefore seems a valid representation of reality. Still, the effects found by allowing friction at the screw-implant and block-implant interfaces are likely not the only cause for the difference in axial displacement between the experimental results and the FE model simulation results, as there still remains a difference of 1.22 mm in axial displacement to be explained.

4.1.2 FE model: screw thread geometry

Another important potential source for the FE model's underestimation of the axial displacement and the implant strains, is the used screw geometry. In current FE studies, it is common to model screws as cylinders with a diameter equal to the nominal thread diameter. This leaves very little room for movement of the implant near the flanges, especially when most or all neighbouring contact interfaces are glued. Inside the screw holes of the implant, the screw geometry is in direct contact with the implant's surface. In reality, however, the screw diameter is only 4.5 mm at this

portion of the screw shaft, so the screw is not in direct contact with the implant (ISO, n.d.). Also, by modelling the screw thread as a cylinder with a diameter equal to the nominal screw thread diameter, a lot of volume is added to the screw. This increase in volume will cause a greater area moment of inertia, consequently increasing the screw's bending stiffness. Furthermore, it may have underestimated the compressive strains in screws 10 and 11, which were positioned right below and oriented in line with the axial loading direction. This would have contributed to the underestimation of the axial displacement by the FE model. For the FE model used in this study, allowing friction with a coefficient of 0.2 at the screw-implant and block-implant interfaces, and modelling the screw thread as a cylinder with a diameter equal to the screw's core diameter of 4.5 mm, yielded a maximum axial displacement of -0.91 mm. This meant an increase in axial displacement of 0.33 mm compared to the same FE model with screws modelled as cylinders with a diameter equal to the nominal screw thread diameter of 6.5 mm.

The type of orthopaedic screw used in this study was a cancellous screw. Not all FE studies report on the specific geometry of the used screw, nor whether it is cancellous or cortical. Cancellous screws have a deep screw thread and a large nominal thread diameter, whereas cortical screws have a shallow screw thread and a small nominal thread diameter (ISO, n.d.). One study specified that the used screw was cortical (Borovkov et al., 2018). Modelling cortical screws with a diameter equal to the nominal screw thread diameter is also done in related applications, like in FE models of dynamic hip screws (Chang, Chen, Li, Peng, & Chang, 2015; W.-P. Chen et al., 2004). Compared to the actual screw geometry, for cortical screws only little volume is added, whereas a lot of volume is added for cancellous screws. Therefore, modelling the screw shaft geometry as a cylinder with a diameter equal to the nominal screw thread diameter seems to be a more valid assumption for cortical screws than cancellous screws. This wrong assumption for the cancellous screw geometry has likely contributed to the FE model's underestimation of the axial displacement.

Something else which was noted when analysing the FE simulation results, was the fact that screws number 10 and 11 on the implant's inner hemispherical surface, see Figure 2.2, were exposed to relatively large (compressive) stresses during the simulation, especially screw 11. This screw is pretty much located right below and in line with the axial loading direction. What makes screws 10 and 11 on the implant's inner hemispherical surface special compared to the other screws at the flanges, is that quite a substantial portion of their shafts was exposed to air and consequently not in direct contact with the Delrin block. This allowed these screws to compress between the parts where they connected to the implant and the block. However, as already mentioned, the assumption of modelling the screw thread as a cylinder

with a diameter equal to the nominal screw thread diameter, adds a lot of volume and bending stiffness to the screws. This may have caused an underestimation of the compressive strains in these screws, consequently contributing to the underestimation of the axial displacement by the FE model.

4.1.3 FE model: cement and cup dimensions

In the original FE model, the outer and inner cement diameters were 54 mm and 50 mm, respectively, and the outer and inner cup diameters were 50 mm and 32 mm, respectively. Therefore, the cement thickness was 2 mm and the cup thickness was 9 mm in the FE model. However, in reality, the nominal cup thickness is 6.9 mm instead of 9 mm (STRYKER, n.d.-a). The cup's outer diameter is defined in the manual based on the cement spacers and not on the outer diameter of the cup's hollow hemisphere (STRYKER, n.d.-a). Therefore, in the experiment, the cement thickness was 4.1 mm and the cup thickness was 6.9 mm. So the outer and inner cement diameters should have been 54 mm and 45.8 mm instead of 54 mm and 50 mm. Also, the outer and inner cup diameters should have been 45.8 mm and 32 mm instead of 50 mm and 32 mm. However, incorporation of these more accurate cement and cup dimensions did not have a large effect on the FE model's axial displacement. The axial displacement was only 0.03 mm less than the previously mentioned -0.91 mm.

4.1.4 Experiment: tightening the screws

During screwing, it was noted that the 3.2 mm diameter milled screw holes were too small. Because of this, some Delrin parts broke under the ischium and pubis flanges. As a result, the ischium and pubis flanges did not make full surface contact with the underlying Delrin surface. The diameter of the milled screw holes was 3.2 mm, the size used for clinically fixing the implant to a patient's pelvic bone. However, for the Delrin block, this diameter was too small because Delrin is much stroger than pelvic bone and because the core diameter of the screw was 4.5 mm (ISO, n.d.). Therefore, the holes had to be predrilled to 3.8 mm. Also, each hole had to be screwed once with a screw to facilitate screwing during final implant placement. It is recommended for future studies that make use of Delrin to create milled holes with a diameter just below the core diameter of the used screw.

Screw number 1 was tightened first, but into a milled 3.2 diameter screw hole. Because

of the high amount of stress exerted on the screw, it broke just below the top of the screw thread at the height of the block surface. It could be expected that this would have increased the experimentally measured axial displacement. However, for the FE model used in this study, allowing friction with a coefficient of 0.2 at the screw-implant and block-implant interfaces, modelling the screw thread as a cylinder with a diameter equal to the screw's core diameter of 4.5 mm, and omitting screw number 1, yielded a maximum axial displacement of -0.93 mm. This meant an increase in axial displacement of 0.02 mm compared to the same model that included screw number 1. The incorporation of the previously mentioned more accurate cement and cup dimensions had no effect on the displacement; it remained -0.93 mm. Thus, the combined effect of the aforementioned changes to the FE model on the axial displacement led to an increase in the maximum axial displacement of 0.5 mm to -0.93 mm, which is more than double the original displacement. However, the difference between the adjusted experimental displacement and the original FE model with all aforementioned changes still remains 0.87 mm, which means that the final FE model reached around half of the adjusted experimental displacement. The regression line for all locations combined, similar to the one shown in Figure 3.3, was computed for this final FE model. The regression equation for this final FE model (FE=0.64·EXP-10.6, R^2=0.85) showed an improved linear correlation with the experimental results compared to the original regression equation (FE=0.32·EXP+54.9, R^2=0.76). The slope of the regression line has doubled from 0.32 to 0.64. The improvement in the FE model's accuracy was mainly caused by the fact that at locations 10, 11, and 12, the simulation results were much more similar to the experimental results than in the original FE model. However, for location 1, the linear correlation had deteriorated.

Although it has been shown that the sum of 1) allowing friction at the screw-implant interface, 2) allowing friction at the block-implant interface, and 3) modelling the screw thread as a cylinder with a diameter equal to the screw's core diameter, seem to have led to a more accurate FE model, they were unable to completely explain the differences between the FE model and experimental results. Therefore, there still remain some causes of the underestimated axial displacement by the FE model to be elucidated.

The effects found by allowing friction at the screw-implant and block-implant interfaces are likely not the only cause for the difference in axial displacement between the experimental results and the FE model simulation results. It could be that the FE model underestimates the effect of omitting screw number 1 because it inaccurately models the behaviour near the screw holes. In the FE model, the screw head geometry perfectly connects to the implant geometry, whereas in the experiment this might not have been the case because of inaccuracies in screw placement. For example, some

screws may have been oriented slightly different from their orientation in the FE model, or their screw heads may not have been entirely in contact with the implant's screw holes. It is likely that these inaccuracies in screw placement in the experiment have also contributed to the increased axial displacement in the experiment compared to the FE model.

4.2 3 mm versus 4 mm thick implant

Apart from the experimental validation of the FE model, another aim of this MSc Thesis project was to compare two implant designs: a 3 mm thick implant and a 4 mm thick implant. The least that could be said about the 3 mm implant's static strength, is the fact that the implant did not fail during the experiment. Therefore, the 3 mm implant design seems to possess sufficient static strength. Of course, the experiment only loaded the implant at a specific angle. Another common extreme loading condition is stumbling, for which forces of 11,000 N were found in a 100 kg subject, and for which the loading direction is similar to walking and walking down the stairs (Bergmann, Bender, Dymke, Duda, & Damm, 2016; OrthoLoad, n.d.). Both the 3 mm and 4 mm implants are expected to perform well under an extreme loading condition like stumbling for a few reasons: 1) The simulations have shown that the reported 99th percentile von Mises stresses were similar for the standing up and down stairs 15 kN loads, 2) an 11,000 N load for stumbling is much less than the 15,000 N load applied in the experiment, and 3) the 99th percentile von Mises stresses remained well below the implant's yield strength for both activities and both implant types at the 15 kN load. However, given that the FE model underestimates most implant strains, it will, consequently, also underestimate most implant stresses. Therefore, it is very likely that the reported percentages in Table 3.2 are an underestimation of the actual values. Yet even if the actual percentages would be a threefold, they would still all be lower than the implant's yield strength. Lastly, the orientations of the maximum resultant force vectors during the standing up activity and the down stairs activity as used in this study, are representative of the orientations of the maximum resultant force vectors of the remaining seven activities available in the HIP98 database (OrthoLoad, n.d.). All in all, it is likely that both implant designs are strong enough to withstand excessive static loads that act in directions that may occur in daily life.

4.3 Future research

During activities of daily living, the implant will primarily be subjected to repetitive and cyclic activities like cycling and walking. Even though the implant's von Mises stresses caused by these cyclic activities may remain below the implant's yield strength, in the long term, fatigue failure will become more and more important. The reported fatigue strength of the 3D printed Ti6Al4V implant used in this study is at least 637 MPa at 10^6 cycles (3DSYSTEMS, n.d.). Future studies could experimentally assess the implant's fatigue stress and identify areas at risk of fatigue failure. Also, some screws might get loose after loading the implant for such a long time. These phenomena are difficult to predict with an FE model.

The clinical performance of the implant could be assessed by performing strain measurements on a cadaveric human pelvis after implant placement. In the current study, a human cadaveric pelvis was not used because it is a weaker material than Delrin, and it would be at risk of failure during the experiment. Also, it would limit the magnitude of the exerted force on the implant, which would hamper the assessment of the implant's static strength and decrease the magnitude of the measured implant strains.

Last but most certainly not least, more research should be done on the FE modelling of orthopaedic screws in revision acetabular components to find out the effects of contact interactions, screw geometries and screw preloading on FE results. This study has already made some suggestions as to how screw modelling may be improved. Future studies should investigate whether allowing friction at the screw-implant and block(or bone)-implant interfaces indeed improves the accuracy of the FE model. Also, studies with similar FE models that incorporate cancellous screws should investigate it is a better assumption to model the screw thread as a cylinder with a diameter equal to the screw's core diameter compared to a diameter equal to the nominal screw thread diameter. Eventually, more accurate simulations of screw mechanics will lead to more accurate FE models, and therefore more accurate predictions of patient-specific implant survival. Also, once an experimentally validated accurate FE model is established, it will be possible to mechanically optimise the implant regarding, for example, thickness, screw positioning, and bone stresses. Furthermore, other types of orthopaedic implants like dynamic hip screws and fixation plates for calcaneal fractures will also benefit from improved FE modelling of orthopaedic screws (Chang et al., 2015; W.-P. Chen et al., 2004; C.-H. Chen et al., 2017). It will greatly improve the overall accuracy of FE simulations of orthopaedic implants where screws are used for implant fixation. Eventually, it will improve implant performance and survival,

as well as the patients' quality of life.

Chapter 5

Conclusion

The main aim of this MSc Thesis project was to assess the static strength of a developed CTAC for use in acetabular component revision surgery in people with severe acetabular bone defect. Also, an attempt was made to experimentally validate an FE model of the developed CTAC. To the author's knowledge, this was the first study that attempted to experimentally validate an FE model of a CTAC. Furthermore, a 3 mm and 4 mm thick implant design were compared.

The developed FE model underestimated the experimentally found axial displacement of the femoral head and most implant strains, especially at the implant's outer hemispherical surface. However, the FE model showed a good linear correlation with the experimental data. It was shown that 1) allowing friction at the screw-implant interface, 2) allowing friction at the block-implant interface, and 3) modelling the screw thread as a cylinder with a diameter equal to the screw's core diameter, managed to increase the axial displacement of the FE model. These changes to the FE model also seem to be a more accurate representation of reality. Even after these changes to the FE model, the final axial displacement still only reached around half of the experimentally found displacement. The causes of the remaining underestimated axial displacement by the FE model remain to be elucidated. This study has stressed the importance of FE model validation for the development of accurate FE models of CTACs and similar orthopaedic implants fixed with screws.

Because the FE model did not seem to be a very accurate representation of the actual stress-state of the implant, the von Mises stresses found by the FE model had to be interpreted with caution. However, the implant did not fail during the experiment. Furthermore, the von Mises stresses for the 3 mm and 4 mm implants remained far

below the implant's yield strength under the simulated extreme loading conditions with 15 kN. Thus, it is likely that both implant designs have sufficient static strength to resist excessive static loads in multiple physiologically relevant directions. All in all, the static strenght analysis of the developed CTAC has shown that the implant has the potential to decrease the high failure rates currently associated with acetabular component revision surgery.

References

3DSYSTEMS. (n.d.). *Laserform ti gr23 (a).* (Accessed from `3d-systems-laserform-ti-gr23(a)-datasheet-us-a4-2020-06-16-a-print.pdf` on 6-14-2022)

ASMINTERNATIONAL. (n.d.). *Volume 2 properties and selection: Nonferrous alloys and special-purpose materials.* (Accessed from `http://sme.vimaru.edu.vn/sites/sme.vimaru.edu.vn/files/volume_2_-_properties_and_selection_nonf.pdf` on 6-14-2022)

Bergmann, G., Bender, A., Dymke, J., Duda, G., & Damm, P. (2016). Standardized loads acting in hip implants. *PloS one*, *11*(5), e0155612.

Borovkov, A., Maslov, L., Zhmaylo, M., Zelinskiy, I., Voinov, I., Keresten, I., ... others (2018). Finite element stress analysis of a total hip replacement in two-legged standing. , *22*(4), 437–458.

Chang, C.-W., Chen, Y.-N., Li, C.-T., Peng, Y.-T., & Chang, C.-H. (2015). Role of the compression screw in the dynamic hip–screw system: A finite-element study. *Medical engineering & physics*, *37*(12), 1174–1179.

Chen, C.-H., Hung, C., Hsu, Y.-C., Chen, C.-S., & Chiang, C.-C. (2017). Biomechanical evaluation of reconstruction plates with locking, nonlocking, and hybrid screws configurations in calcaneal fracture: a finite element model study. *Medical & biological engineering & computing*, *55*(10), 1799–1807.

Chen, W.-P., Tai, C.-L., Shih, C.-H., Hsieh, P.-H., Leou, M.-C., & Lee, M. S. (2004). Selection of fixation devices in proximal femur rotational osteotomy: clinical complications and finite element analysis. *Clinical Biomechanics*, *19*(3), 255–262.

Chiarlone, F., Zanirato, A., Cavagnaro, L., Alessio-Mazzola, M., Felli, L., & Burastero, G. (2020). Acetabular custom-made implants for severe acetabular bone defect in revision total hip arthroplasty: a systematic review of the literature. *Archives of Orthopaedic and Trauma Surgery*, *140*(3), 415–424.

Dall'Ava, L., Hothi, H., Di Laura, A., Henckel, J., & Hart, A. (2019). 3d printed acetabular cups for total hip arthroplasty: a review article. *Metals*, *9*(7), 729.

De Martino, I., Strigelli, V., Cacciola, G., Gu, A., Bostrom, M. P., & Sculco, P. K.

(2019). Survivorship and clinical outcomes of custom triflange acetabular components in revision total hip arthroplasty: a systematic review. *The Journal of Arthroplasty*, *34*(10), 2511–2518.

Doczi, M. O., Szoedy, R., & Zwierczyk, P. T. (2020). Failure analysis of a custom-made acetabular cage with finite element method. In *Ecms* (pp. 250–255).

Dong, E., Wang, L., Iqbal, T., Li, D., Liu, Y., He, J., ... Li, Y. (2018). Finite element analysis of the pelvis after customized prosthesis reconstruction. *Journal of Bionic Engineering*, *15*(3), 443–451.

DSGROUP. (n.d.). *Eigenschappen kunststoffen.* (Accessed from `https://www.ds-groep.nl/files/downloads/eigenschappen-kunststoffen.pdf` on 6-14-2022)

Du Preez, W., Monaheng, L., Haupt, P., & Olwagen, A. (2016). Strain gauge validation of finite element analysis of a ti6al4v (eli) mandibular implant produced through additive manufacturing..

Fu, J., Ni, M., Chen, J., Li, X., Chai, W., Hao, L., ... Zhou, Y. (2018). Reconstruction of severe acetabular bone defect with 3d printed ti6al4v augment: a finite element study. *BioMed Research International*, *2018*.

Hsu, J.-T., Chang, C.-H., Huang, H.-L., Zobitz, M. E., Chen, W.-P., Lai, K.-A., & An, K.-N. (2007). The number of screws, bone quality, and friction coefficient affect acetabular cup stability. *Medical engineering & physics*, *29*(10), 1089–1095.

Innocenti, B., Bilgen, Ö. F., Labey, L., Van Lenthe, G. H., Vander Sloten, J., & Catani, F. (2014). Load sharing and ligament strains in balanced, overstuffed and understuffed uka. a validated finite element analysis. *The Journal of arthroplasty*, *29*(7), 1491–1498.

Inzana, J. A., Varga, P., & Windolf, M. (2016). Implicit modeling of screw threads for efficient finite element analysis of complex bone-implant systems. *Journal of biomechanics*, *49*(9), 1836–1844.

ISO. (n.d.). *Iso 5835:1991(en) implants for surgery — metal bone screws with hexagonal drive connection, spherical under-surface of head, asymmetrical thread — dimensions.* (Accessed from `https://www.iso.org/obp/ui/#iso:std:iso:5835:ed-1:v1:en` on 6-9-2022)

Kadkhodapour, J., Montazerian, H., Darabi, A. C., Anaraki, A., Ahmadi, S., Zadpoor, A., & Schmauder, S. (2015). Failure mechanisms of additively manufactured porous biomaterials: Effects of porosity and type of unit cell. *Journal of the mechanical behavior of biomedical materials*, *50*, 180–191.

Kaku, N., Hara, K., Tabata, T., & Tsumura, H. (2015). Influence of the volume of bone defect, bone grafting methods, and hook fixation on stress on the kerboull-type plate and screw in total hip arthroplasty: three-dimensional finite element analysis. *European Journal of Orthopaedic Surgery & Traumatology*, *25*(2), 321–329.

Karachalios, T., Komnos, G., & Koutalos, A. (2018). Total hip arthroplasty: survival and modes of failure. *EFORT open reviews*, *3*(5), 232–239.

Lee, C. (n.d.). *Properties of bone cement: The mechanical properties of pmma bone cement.* (Accessed from http://eknygos.lsmuni.lt/springer/483/60-66.pdf on 6-14-2022)

Lie, S., Havelin, L., Furnes, O., Engesaeter, L., & Vollset, S. (2004). Failure rates for 4762 revision total hip arthroplasties in the norwegian arthroplasty register. *The Journal of Bone and Joint Surgery. British volume*, *86*(4), 504–509.

Malito, L. G., Arevalo, S., Kozak, A., Spiegelberg, S., Bellare, A., & Pruitt, L. (2018). Material properties of ultra-high molecular weight polyethylene: Comparison of tension, compression, nanomechanics and microstructure across clinical formulations. *Journal of the Mechanical Behavior of Biomedical Materials*, *83*, 9–19.

Maslov, L., Surkova, P., Maslova, I., Solovev, D., Zhmaylo, M., Kovalenko, A., & Bilyk, S. (2019). Finite-element study of the customized implant for revision hip replacement. *Vibroengineering Procedia*, *26*, 40–45.

Medical, M. (n.d.). *Patient-specific 3d-printed amace hip implant — acetabular revision system — materialise medical.* (Accessed from https://www.youtube.com/watch?v=XIQEjtm-aXc on 6-9-2022)

Micro-Measurements. (n.d.-a). *361a-20r-25 solder, tin-lead-antimony (25 ft).* (Accessed from https://micro-measurements.com/pca/detail/361a20r25-solder-tinleadantimony-25-ft on 6-9-2022)

Micro-Measurements. (n.d.-b). *Cea-062uwa-350 data sheet.* (Accessed from https://datasheet.lcsc.com/lcsc/1912111437_Vishay-Micro-Measurements-CEA-06-062UWA-350_C404310.pdf on 6-9-2022)

Micro-Measurements. (n.d.-c). *Csp-1 cotton swabs (pkg of 100).* (Accessed from https://micro-measurements.com/pca/detail/csp1-cotton-swabs-pkg-of-100 on 6-9-2022)

Micro-Measurements. (n.d.-d). *Gc-6 isopropyl alcohol (4 oz bottle).* (Accessed from https://micro-measurements.com/pca/detail/gc6-isopropyl-alcohol-4-oz-bottle on 6-9-2022)

Micro-Measurements. (n.d.-e). *General information and selection.* (Accessed from http://www.vishaypg.com/docs/11021/insttool.pdf on 6-9-2022)

Micro-Measurements. (n.d.-f). *Gsp-1 gauze sponges (pkg of 200).* (Accessed from https://micro-measurements.com/pca/detail/gsp1-gauze-sponges-pkg-of-200 on 6-9-2022)

Micro-Measurements. (n.d.-g). *M-bond 200 kit.* (Accessed from https://micro-measurements.com/pca/detail/mbond-200-kit on 6-9-2022)

Micro-Measurements. (n.d.-h). *Mca-1 m-prep conditioner a (2 oz bottle).* (Accessed from https://micro-measurements.com/pca/detail/mca1-mprep-conditioner-a-2-oz-bottle on 6-9-2022)

Micro-Measurements. (n.d.-i). *M-coat a polyurethane (four 1 oz bottle).* (Accessed from https://micro-measurements.com/pca/detail/mcoat-a-polyurethane-four-1-oz-bottle on 6-9-2022)

Micro-Measurements. (n.d.-j). *Mn5a-1 m-prep neutralizer 5a (2 oz bottle).* (Accessed from https://micro-measurements.com/pca/detail/mn5a1-mprep-neutralizer-5a-2-oz-bottle on 6-9-2022)

Micro-Measurements. (n.d.-k). *Rsk-4 rosin solvent (four 1 oz bottle).* (Accessed from https://micro-measurements.com/pca/detail/rsk4-rosin-solvent-four-1-oz-bottle on 6-9-2022)

Micro-Measurements. (n.d.-l). *Scp-1 silicon carbide paper, 220 grit (1 in x 100 ft).* (Accessed from https://micro-measurements.com/pca/detail/scp1-silicon-carbide-paper-220-grit-1-in-x-100-ft on 6-9-2022)

Micro-Measurements. (n.d.-m). *Scp-2 silicon carbide paper, 320 grit (1 in x 100 ft).* (Accessed from https://micro-measurements.com/pca/detail/scp2-silicon-carbide-paper-320-grit-1-in-x-100-ft on 6-9-2022)

Micro-Measurements. (n.d.-n). *Strain gage installations with m-bond 200 adhesive.* (Accessed from http://www.vishaypg.com/docs/11127/11127B127.pdf on 6-9-2022)

Micro-Measurements. (n.d.-o). *Strain gage selection: Criteria, procedures, recommendations.* (Accessed from http://www.vishaypg.com/docs/11055/tn505.pdf on 16-9-2022)

Moussa, A., Rahman, S., Xu, M., Tanzer, M., & Pasini, D. (2020). Topology optimization of 3d-printed structurally porous cage for acetabular reinforcement in total hip arthroplasty. *Journal of the Mechanical Behavior of Biomedical Materials*, *105*, 103705.

Orr, J., Dunne, N., & Quinn, J. (2003). Shrinkage stresses in bone cement. *Biomaterials*, *24*(17), 2933–2940.

OrthoLoad. (n.d.). *Data collection 'hip98'.* (Accessed from https://orthoload.com/test-loads/data-collection-hip98/ on 6-8-2022)

PG, V. (n.d.). *Surface preparation for strain gage bonding.* (Accessed from http://www.vishaypg.com/docs/11129/11129_b1.pdf on 6-9-2022)

Plessers, K., & Mau, H. (2016). Stress analysis of a burch-schneider cage in an acetabular bone defect: A case study. *Reconstructive review*, *6*(1).

Sheth, N. P., Nelson, C. L., Springer, B. D., Fehring, T. K., & Paprosky, W. G. (2013). Acetabular bone loss in revision total hip arthroplasty: evaluation and management. *JAAOS-Journal of the American Academy of Orthopaedic Surgeons*, *21*(3), 128–139.

SmithandNephew. (n.d.). *Oxinium™ femoral heads.* (Accessed from https://www.smith-nephew.com/documents/italy/ibooks/adr/oxinium%20femoralheads%20brochure_71380915.pdf on 6-27-2022)

SPACEMATDB. (n.d.). *Delrin design information.* (Accessed from https://www.spacematdb.com/spacemat/manudatasheets/Delrin%20design%20info.pdf on 6-14-2022)

Speelman, L., Bosboom, E., Schurink, G., Hellenthal, F., Buth, J., Breeuwer, M., ... van de Vosse, F. (2008). Patient-specific aaa wall stress analysis: 99-percentile versus peak stress. *European Journal of Vascular and Endovascular Surgery*, *36*(6), 668–676.

STRYKER. (n.d.-a). *Exeter rimfit x3 acetabular cup surgical technique.* (Accessed from https://www.strykermeded.com/media/1702/exeter-x3-rimfit-surgical-technique.pdf on 6-16-2022)

STRYKER. (n.d.-b). *Simplex bone cement.* (Accessed from https://www.strykermeded.com/medical-devices/surgical-solutions/surgical-equipment/simplex-bone-cement/ on 6-16-2022)

SYNTHES. (n.d.). *Synthes 6.5mm cancellous bone screw titanium.* (Accessed from https://e-katalog.lkpp.go.id/public/files/upload/produk_lampiran/2017/10/26/15090024864854.pdfon 6-16-2022)

Wieding, J., Souffrant, R., Fritsche, A., Mittelmeier, W., & Bader, R. (2012). Finite element analysis of osteosynthesis screw fixation in the bone stock: an appropriate method for automatic screw modelling. *PloS one*, *7*(3), e33776.

Zhang, Q.-H., Wang, J.-Y., Lupton, C., Heaton-Adegbile, P., Guo, Z.-X., Liu, Q., & Tong, J. (2010). A subject-specific pelvic bone model and its application to cemented acetabular replacements. *Journal of biomechanics*, *43*(14), 2722–2727.

Chapter 6

Appendix

6.1 Surface preparation and strain gauge installation

For measuring implant strains with strain gauges, it is important to prepare the implant surface for strain gauge application. Here, the surface preparation steps as described in Micro-Measurements' Instruction Bulletins B-127 and B-129-8 were followed precisely (Micro-Measurements, n.d.-n; PG, n.d.). First, the 3D printed implant was dry abraded by hand with 120-grit sandpaper on the ilium flange and the outer hemispherical surface. A piece of sandpaper was attached with double-sided tape to a flat wooden stick to facilitate abrasion near hard-to-reach areas, e.g. near the screw holes of the ilium flange. This process was continued until little pits and bumps were invisible with the eye on the surfaces where the strain gauges would later be applied on. To remove oils from the titanium surface, it was required to heat-cycle the specimen three times to 175 °C (PG, n.d.). A single heat cycle entailed the heating of the implant to 175 °C in an oven, allowing it to cool down to room temperature, and degreasing the implant with alcohol. The remaining steps for the surface preparation included the following five general steps (PG, n.d.):

1. Solvent degreasing
2. Dry and wet abrading
3. Application of gauge layout lines

4. Conditioning
5. Neutralising

The following materials were used to complete the aforementioned steps:

- GC-6 isopropyl alcohol (Micro-Measurements, n.d.-d)
- GSP-1 gauze sponges (Micro-Measurements, n.d.-f)
- SCP-1 220-grit silicon-carbide paper (Micro-Measurements, n.d.-l)
- SCP-2 320-grit silicon-carbide paper (Micro-Measurements, n.d.-m)
- MCA-1 M-Prep Conditioner A (Micro-Measurements, n.d.-h)
- strain gauge placement guides
- MN5A-1 M-Prep Neutraliser 5A (Micro-Measurements, n.d.-j)
- CSP-1 cotton swabs (Micro-Measurements, n.d.-c)

After heat-cycling the implant, the entire gauging area was again degreased with GC-6 isopropyl alcohol and a GSP-1 gauze sponge. Generally, CSM Degreaser is preferred, but titanium and many plastics react with strong solvents, which is why GC-6 isopropyl alcohol was used. Next, the surface was dry abraded with SCP-1 220-grit silicon-carbide paper and wet abraded with SCP-2 320-grit silicon-carbide paper. During wet abrasion, the surface was kept thoroughly wet by the application of MCA-1 M-Prep Conditioner A. Wet abrasion was concluded by wiping the surface dry with a gauze sponge. Two 3D printed polyamide (Oceanz, Ede, The Netherlands) strain gauge placement guides were used for applying pairs of crossed layout lines at the points where the strain measurements were to be made, see Figure 2.5. The locations and orientations of the strain gauges were chosen based on the FE simulation results of the magnitude and orientation of the maximum principal elastic strains. The locations corresponded to nodes at which relatively high maximum principal elastic strain values were expected. The orientations of the strain gauges were such that they aligned with the expected direction of the maximum principal elastic strain. The placement guides contained cruciform notches that served to define the locations and the orientations of all 12 strain gauges. The intersection of the two perpendicular lines corresponded to the centre of the measuring grid of the strain gauge, which is

where the strain measurement is made. A propelling pencil was repeatedly moved back and forth along both notches until two lines were clearly visible. After removal of the placement guide, the surface was scrubbed with a CSP-1 cotton swab whilst MCA-1 M-Prep Conditioner A was repeatedly applied to keep the surface wet. The surface was deemed sufficiently clean once a clean tip was no longer discoloured by the rubbing. A clean GSP-1 gauze sponge was wiped through the gauge area with a single stroke to dry the surface. Finally, MN5A-1 M-Prep Neutraliser 5A was applied to the surface whilst scrubbing the surface with a CSP-1 cotton swab. A single stroke of a GSP-1 gauze sponge through the neutralised area concluded the surface preparation step.

Strain gauge installation

For titanium test materials, it is important to install the strain gauges within 10 minutes of the final surface preparation step, i.e. the surface neutralisation step (PG, n.d.). The following materials were used to install the strain gauges:

- tweezers
- glass plate
- PCT-3M gauge installation tape (Micro-Measurements, n.d.-e)
- CEA-06-062UWA-350 strain gauges (Micro-Measurements, n.d.-b)
- ilium strain gauge placement guide
- outer hemisphere strain gauge placement guide
- M-Bond 200 kit catalyst (Micro-Measurements, n.d.-g)
- M-Bond 200 kit adhesive (Micro-Measurements, n.d.-g)
- GSP-1 gauze sponges (Micro-Measurements, n.d.-f)
- 361A-20R-25 solder (Micro-Measurements, n.d.-a)
- soldering iron station (WELLER WECP-20, The Cooper Group GmbH, Besigheim, Germany)
- RSK-4 rosin solvent (Micro-Measurements, n.d.-k)

- connecting wires
- M-Coat A Polyurethane (Micro-Measurements, n.d.-i)

The type of strain gauge that was used for the experiment was CEA-06-062UWA-350. One of the most important characteristics of a strain gauge is its gauge length. CEA-06-062UWA-350 strain gauges have a gauge length of 62 mils, i.e. 0.062 inch or 1.57 mm. The gauge length should be no greater than 0.1 times the radius of the surface at which the strain measurement is to be made (Micro-Measurements, n.d.-o). The implant's outer hemispherical surface has a radius of 30 mm, so the gauge length should be no greater than $0.1 \cdot 30$ mm $= 3$ mm. The first available gauge length smaller than 3 mm was 62 mils. The radius of the ilium flange surface is much greater than the radius of the outer hemispherical surface, so the gauges can be readily applied on the ilium too. This type of strain gauge was also advised by an authorized strain gauge manufacturer for application on a titanium surface. This type of strain gauge has a grid resistance of $350.0 \pm 0.2\%$ Ω, a gauge factor of $2.120 \pm 0.5\%$, and a strain range of 3%. All strain gauges were checked on their grid resistance with an ohmmeter (FLUKE 77 MULTIMETER, Fluke Corporation, Everett, WA, USA), and all were found to be 350 Ω. For strain gauge installation, the gauge was first placed with tweezers on a clean glass plate with the bonding side down. A 150-mm piece of PCT-3M gauge installation tape was placed over the gauge. Then, the gauge was centred on the perpendicular layout lines. The placement guide was placed over the tape to verify the strain gauge position and orientation. The strain gauge was repositioned if needed. The gauge was brought up at the gauge end until the tape was lifted 1 cm beyond the solder tabs. The loose tape end was tucked under, and the specimen was pressed to enforce that the gauge remained flat. A thin and uniform layer of M-Bond 200 catalyst was applied to the bonding surface of the gauge. It was let dry for 1 minute. Finally, two drops of M-Bond adhesive were applied at the junction of the tape and specimen area. Immediately thereafter, the tape was rotated and held slightly stretched, while a GSP-1 gauze sponge was slowly and firmly wiped over the tape in a single stroke. Firm thumb pressure was applied to the gauge for at least two minutes. All strain gauges were installed in one day. The next day, all tape was removed by slowly and steadily pulling the tape back directly over itself. The gauges were then soldered to connecting wires with RSK-4 rosin solvent. Each connecting wire was marked with a number corresponding to the strain gauge number it was connected to. The last step was the application of M-Coat A Polyurethane, which is a protective coating, on the strain gauge and the connecting wires.